RESEARCH ARTICLE

WILEY

LIDAR-assisted feedforward individual pitch control of a 15 MW floating offshore wind turbine

Andrew J. Russell[1] | Maurizio Collu[2] | Alasdair S. McDonald[3] |
Philipp R. Thies[4] | Aidan Keane[5] | Alexander R. Quayle[6]

[1]Industrial Doctoral Centre for Offshore Renewable Energy, School of Engineering, King's Buildings, University of Edinburgh, Edinburgh, UK

[2]Department of Naval Architecture, Ocean and Marine Engineering, University of Strathclyde, Glasgow, UK

[3]School of Engineering, King's Buildings, University of Edinburgh, Edinburgh, UK

[4]Faculty of Environment, Science and Economy Engineering, University of Exeter, Penryn Campus, Penryn, UK

[5]Wood Renewables, Glasgow, UK

[6]Flotation Energy Ltd, Edinburgh, UK

Correspondence
Andrew J. Russell, Industrial Doctoral Centre for Offshore Renewable Energy, School of Engineering, King's Buildings, University of Edinburgh, Edinburgh EH9 3JL, UK.
Email: A.J.Russell-1@sms.ed.ac.uk

Abstract

Nacelle-mounted, forward-facing light detection and ranging (LIDAR) technology can deliver benefits to rotor speed regulation and loading reductions of floating offshore wind turbines (FOWTs) when assisting with blade pitch control in above-rated wind speed conditions. Large-scale wind turbines may be subject to significant variations in structural loads due to differences in the wind profile across the rotor-swept area. These loading fluctuations can be mitigated by individual pitch control (IPC). This paper presents a novel LIDAR-assisted feedforward IPC approach that uses each blade's rotor azimuth position to allocate an individual pitch command from a multi-beam LIDAR. In this study, the source code of OpenFAST wind turbine modelling software was modified to enable LIDAR simulation and LIDAR-assisted control. The LIDAR simulation modifications were accepted by the National Renewable Energy Laboratory (NREL) and are now present within OpenFAST releases from v3.5 onwards. Simulations of a 15 MW FOWT were performed across the above-rated wind spectrum. Under a turbulent wind field with an average wind speed of 17 ms^{-1}, the LIDAR-assisted feedforward IPC delivered up to 54% reductions in the root mean squared errors and standard deviations of key FOWT parameters. Feedforward IPC delivered enhancements of up to 12% over feedforward collective pitch control, relative to the baseline feedback controller. The reductions to the standard deviation and range of the rotor speed may enable structural optimization of the tower, while the reductions in the variations of the loadings present an opportunity for reduced fatigue damage on turbine components and, consequently, a reduction in maintenance expenditure.

KEYWORDS
feedforward control, individual pitch control, LIDAR-assisted control, nacelle-mounted LIDAR

1 | INTRODUCTION

The application of light detection and ranging (LIDAR) technology for assisting wind turbine control is gathering momentum in its path towards commercialization. Nacelle-mounted, forward-facing LIDAR can provide measurements of the incoming wind field, the characteristics of which

can be used for feedforward turbine control. Traditionally, wind turbine control strategies have utilized feedback control, which updates the controller settings following the impact of the incoming disturbance. However, the drawback of this type of control strategy is that the wind turbine controller provides a delayed reaction to the incoming wind. Feedforward control overcomes this drawback by enabling turbines to actuate their torque, pitch or yaw systems in advance of the wind's impact upon the rotor.

According to the existing literature, the greatest benefits delivered by LIDAR-assisted control have been achieved when assisting with blade pitch control in above-rated wind speed conditions.[1–3] LIDAR-assisted feedforward pitch control can enhance turbine performance through improved rotor speed regulation and therefore more stable power capture. It is also capable of reducing the variation in the structural loadings, which has the potential to reduce the levelized cost of offshore wind energy by extending maintenance intervals and the lifetime of wind turbines.

Floating offshore wind turbines (FOWTs) are able to capture wind power from further distances offshore, where waters are too deep for the use of bottom-fixed turbines. However, as FOWTs are subject to softer foundation properties, their control systems have to be designed differently from their bottom-fixed counterparts, primarily to prevent negative aerodynamic damping as a consequence of unfavourable coupling between the platform's motion and the blade pitch controller in above-rated wind speeds.[4,5] These modifications give rise to greater rotor speed variation of FOWTs compared to bottom-fixed turbines,[4,6] resulting in larger rotor rotational (1P) and blade passing (3P) frequency ranges, and leading to the requirement for larger, stiffer turbine towers.

Within the literature, LIDAR-assisted pitch control has also demonstrated its ability to deliver reductions to the variations of the rotor speed, structural loads and platform motions of FOWTs. Studies have focused on FOWTs using spar-buoy[1] and tension-leg platform[2] foundations supporting NREL's 5 MW reference turbine, as defined by Jonkman et al,[7] and semi-submersible foundations for a 10 MW turbine model.[3] By 2024, turbines of up to 16 MW capacity will be commercially available.[8] Studies have now begun to predict the benefits attainable for these large floating turbines through simulations of LIDAR-assisted pitch control applied to the International Energy Agency (IEA)-Wind 15 MW reference turbine[9] mounted on the University of Maine's VolturnUS-S[10] semi-submersible platform.[11,12]

Individual pitch control (IPC) aims to mitigate the cyclic loads experienced by wind turbines due to variations in the wind profile across the rotor-swept area caused by wind shear, wind veer and turbulence. The concept of feedback IPC (FBIPC) was first explored by Bossanyi[13] and applied to floating turbines by Namik and Stol.[14] Within this strategy, the individual controller requires the three out-of-plane blade root bending moments and the rotor azimuth as feedback inputs to allow for the derivation of a pitch command for each blade, which adds to the command provided by the collective pitch controller.

Alternatively, feedforward individual pitch control (FFIPC) is able to deliver individual pitch commands in advance of the wind's impact and has been studied using various implementations.[15–18] Schlipf et al[15] used H_∞ optimization to design an individual pitch controller using a linear time-invariant (LTI) model. Raach et al[16] used a non-linear model predictive controller (NMPC) to deliver individual blade feedforward commands to a 5 MW floating wind turbine. Dunne et al[17,18] studied a LIDAR whose beams rotated with the blades and was used to assign a command to each blade using the same proportional–integral (PI) controller as was used for the collective pitch controller. The LIDAR used three wind speed inputs, one at each blade, at approximately 75% span to deliver the individual commands and resulted in improvements over the baseline feedback individual pitch controller.[18] Studies are yet to investigate the benefits of LIDAR-assisted FFIPC of large (15 MW+) FOWTs, whose rotor diameters are approaching 250 m. These large diameters will give rise to greater variations in the wind speed across the rotor-swept area, leading to significant variations in the loadings on the turbine's structures.

This paper aims to quantify the performance improvements and motion and loading reductions achievable through simulations of LIDAR-assisted pitch control of a 15 MW semi-submersible FOWT in above-rated wind speed conditions. The source code of OpenFAST wind turbine modelling software was modified to allow for the simulation of nacelle-mounted LIDAR wind velocity measurement. These modifications were accepted by NREL and are now present within OpenFAST releases from v3.5[19] onwards. Furthermore, the LIDAR measurements were interfaced with OpenFAST's control framework to enable LIDAR-assisted control within the Reference Open-Source Controller (ROSCO),[20] which was also modified within this work. A multi-beam LIDAR was simulated to enable calculation of the rotor-effective wind speed (REWS), representing the average wind speed across the rotor-swept area. The REWS was used by the implemented feedforward controller, which included collective pitch control (CPC) and IPC capabilities. The FFIPC approach used the rotor azimuth position of each blade to allocate an appropriate individual pitch command, which was combined with the command provided by the feedforward-feedback collective pitch controller (FFCPC). The time series performance of the FFCPC, the FFCPC with traditional FBIPC (FFCPC + FBIPC) and the FFCPC with feedforward IPC (FFCPC + FFIPC) was compared to that of the traditional feedback-only collective pitch controller (FB), which was used as the baseline. The impact of the rotor radius percentage span locations of the LIDAR beams on the performance of the FFCPC + FFIPC was also assessed. Performance benefits were quantified through comparison of normalized values of key performance metrics of various turbine and substructure parameters.

The paper is outlined as follows: Section 2 describes the modelling software, turbine and substructure models analysed. Section 3 outlines the modifications made to the OpenFAST and ROSCO source code to enable LIDAR measurement and feedforward control. Section 4 details the

feedback and feedforward collective and individual pitch control theory. Section 5 describes the simulation setup and the key statistical metrics. Section 6 outlines the results, provides discussion on them and details the limitations of the study, and Section 7 offers conclusions from the study and the next steps of the research.

2 | TURBINE–SUBSTRUCTURE MODELLING

This section provides information regarding the software, turbine and supporting structure used when performing the simulations.

The numerical modelling tool employed for this study was NREL's open-source Fatigue, Aerodynamics, Structures, and Turbulence (FAST) code. This software is classed as an aero-hydro-servo-elastic tool for the modelling of full non-linear wind turbine models. It allows for the intricate specification of the turbine's design, external environment (wind, wave and current conditions) and controller. OpenFAST is the latest iteration of the FAST code and v3.4 was the original (before modifications) version of the program used in this study.[21]

2.1 | Turbine and support structure models

2.1.1 | Turbine

The turbine studied in this work was the IEA-Wind 15 MW reference turbine, developed between NREL and the Technical University of Denmark (DTU), via the IEA, as defined by Gaertner et al.[9] The specifications of the reference turbine are given in Table 1.

The turbine rotor operates with a minimum rotational speed of 5 rpm to avoid 3P interference with the tower/monopile natural frequencies[9] and reaches a rated rotational speed of 7.56 rpm at 10.59 ms^{-1}. The blades begin pitching at the rated wind speed in order to maintain the rotor rotation at its rated speed.

2.1.2 | Substructure

The floating substructure model utilized for this work was the University of Maine (UMaine) VolturnUS-S semi-submersible,[10] designed to support the IEA 15 MW reference turbine. Key specifications of the substructure are shown in Table 2.

TABLE 1 Parameters of the IEA-Wind 15 MW reference turbine.[9]

Parameter	Value	Units
Power rating	15	MW
Turbine class	IEC Class B	-
Cut-in wind speed	3	ms^{-1}
Rated wind speed	10.59	ms^{-1}
Cut-out wind speed	25	ms^{-1}
Minimum rotor speed	5.00	rpm
Maximum rotor speed	7.56	rpm
Rotor diameter	240	m
Hub height	150	m
Drive train	Direct drive	-

TABLE 2 Parameters of the VolturnUS-S semi-submersible model.[10]

Parameter	Value	Units
Material	Steel	-
Draft	20	m
Mass (including ballast)	17,839	kg
Mooring system	Three line catenary	-

2.1.3 | Tower

The towers of FOWTs are required to have higher stiffness characteristics than bottom-fixed configurations due to increased inertial and gravity loads resulting from platform motions.[10] Therefore, the tower for the VolturnUS-S was designed separately from the configuration of the monopile outlined by Gaertner et al.[9] The tower was designed to have its first fore–aft and side-to-side natural frequencies outside of the 1P and 3P ranges. The 1P and 3P ranges were modified for the 15 MW turbine on the VolturnUS-S to account for the increased rotor speed variation caused by the platform motions. Therefore, a stiff-stiff tower, with first natural frequencies above 3P was required because of a very narrow soft-stiff range between 1P and 3P when additional safety factors were applied.[10] Further detail on the tower design for the 15 MW VolturnUS-S can be found within its definition document.[10]

3 | INTEGRATION OF LIDAR SIMULATION AND FEEDFORWARD CONTROL WITHIN OPENFAST

In the original version of OpenFAST v3.4 used in this study, LIDAR simulation was not possible within the program itself. Work has been conducted by Schlipf et al[22] and Guo et al[23] to develop an additional LIDAR simulator module to be called by the OpenFAST input file, with an additional .dll chain created for interface with the ROSCO controller. However, within this work, a LIDAR simulator has been developed that is integrated within the original OpenFAST framework. Here, LIDAR simulation is incorporated within the InflowWind module. The modifications made to OpenFAST (as will be outlined in Section 3.1) were proposed to NREL via a GitHub pull request. They were subsequently accepted and are present in the latest release of the program, v3.5.[19] The LIDAR measurements are linked with ServoDyn to enable interface with the modified ROSCO controller, developed to include LIDAR-assisted control. This section outlines the modifications made to the OpenFAST and ROSCO source code to allow for the integration of LIDAR simulation and LIDAR-assisted control.

3.1 | Integration of LIDAR simulation within InflowWind

As the InflowWind module of OpenFAST specifies the input wind conditions, it was identified as the point of integration of the LIDAR model. This was achieved through modification and addition to the source code, written in Fortran. Firstly, the source code was modified to allow for the LIDAR parameters and configuration to be specified within the InflowWind input file, allowing for customization by the user. The input files are then parsed and saved as parameters within the source code to be used within the program.

The LIDAR beam(s) can be configured in multiple ways. Single-point beam(s) can be configured where focal distances can be specified independently for each beam (as is the case in this study). Alternatively, a single beam can be configured in a continuous or pulsed manner. In the continuous mode, a single focal distance is configured, whereas, in the pulsed mode, measurements can be taken at multiple range gates. In both continuous and pulsed configurations, the beam is modelled as a Gaussian beam, whereby a weighting function defines the probe length at the focal point. The measurement frequency can also be specified. Additionally, the simulator can account for the impacts of platform motions on the movement of the nacelle, which are extracted from the ElastoDyn module. These can be used to modify the measurement coordinates of the LIDAR beam(s). The simulator considers the displacements in the x, y and z directions, though does not account for velocities, accelerations or rotations. The authors are aware that these omissions may lead to an overestimation of the LIDAR preview quality, which will be investigated in future work. For example, the preview quality can be affected by the linear velocity of the LIDAR, which will be included within the Doppler effect, and so, in this case, a motion compensation algorithm will be required to remove the contribution of the LIDAR velocity from the LOS speed measurement.

The LIDAR device's wind speed measurements are taken from the wind field provided to InflowWind such as those generated by TurbSim. The LIDAR's wind speed measurements can be outputted from the InflowWind module for user analysis and interface with other modules, such as ServoDyn, for LIDAR-assisted control.

In a real LIDAR system, each measurement consists of a measurement of the projection of the wind velocity vector onto a LIDAR beam direction, referred to as the line-of-sight (LOS) velocity, at selected points along the beam direction. The wind velocity vector is then determined through the wind field reconstruction (WFR) method, which is based upon trigonometric considerations.[22–24] In this work, the wind field is modelled as a horizontally homogeneous inflow. The single-point LIDAR beams are assumed to be perfectly aligned with the wind direction and are also assumed to not rotate during the simulations, meaning that the LIDAR beam directions are maintained in their orientations with respect to the horizontal plane. It follows that the transverse components of the wind field are assumed to be zero in the LIDAR frame of reference. This means that the wind field at a point can be determined from a single longitudinal velocity measurement, and sidesteps the need to conduct a full WFR under the current setup. In addition, it has been assumed that the wind velocity does not change from the point of measurement to the rotor, therefore assuming Taylor's frozen hypothesis.[25] In reality, the wind velocity would evolve in this interval, though previous studies have

considered the wind evolution and found it to not be significantly impactful on the performance of LIDAR-assisted control, and that a simple linear filter design for LIDAR-assisted control is sufficient for various atmospheric stability conditions.[24]

3.2 | Interface of LIDAR measurement to ROSCO

ServoDyn is the module within OpenFAST responsible for defining control inputs and outputs and calling to the requested controller interface, which is typically a .dll file, namely, ROSCO. As ROSCO is compiled to a .dll using a separate Fortran solution to OpenFAST, an interface between the two is required so that inputs and outputs can be transferred. Within OpenFAST, this is achieved using the avrSWAP array, which is constructed within ServoDyn.

To achieve interface to the ServoDyn module from InflowWind, the LIDAR-measured wind speed outputs of the InflowWind module had to be specified as inputs within the ServoDyn module's source code, and these could then be added to the avrSWAP array to be sent to ROSCO.

The LIDAR-assisted collective pitch controller was created by adding an additional feedforward control subroutine within the ROSCO source code. The pitch controller calls the feedforward control script to compute the outputs to be sent to the feedforward-feedback controller for the determination of the pitch command. If individual feedforward pitch control is enabled, a further separate subroutine is called to compute the individual commands to be assigned to each blade.

4 | PITCH CONTROLLER THEORY

4.1 | Feedback pitch controller

The baseline feedback pitch controller used the default ROSCO inputs for the 15 MW VolturnUS-S,[10] accessible from GitHub.[26] It utilizes a gain-scheduled PI pitch controller, with gains detuned from the bottom-fixed version to prevent undesirable coupling between the blade pitch control actuation frequency and the floating platform rigid-body pitch oscillation natural frequency.[10] The feedback pitch controller requires the generator's rotational speed as the feedback input. The error (e_{FB}) between the low-pass filtered generator rotational speed (Ω_g) and the rated generator rotational speed ($\Omega_{g,rated}$) is first calculated as

$$e_{FB} = \Omega_{g,rated} - \Omega_g. \tag{1}$$

The proportional component of the feedback controller (P_{FB}) is then calculated through multiplication of e_{FB} with a scheduled (according to the blade pitch angle) proportional gain term (K_p)

$$P_{FB} = K_p e_{FB}. \tag{2}$$

The integral component of the feedback controller (I_{FB}) is calculated through multiplication of e_{FB} with the time step duration (Δt) and the gain-scheduled integral gain (K_I), which is added to the previous feedback integral component ($I_{FB,prev}$)

$$I_{FB} = I_{FB,prev} + \Delta t K_I e_{FB}. \tag{3}$$

The feedback pitch command (θ_{FB}) is determined through combination of P_{FB} and I_{FB}:

$$\theta_{FB} = P_{FB} + I_{FB}. \tag{4}$$

For floating turbines, an additional pitch command is provided through consideration of the nacelle rotational velocity to aid in overcoming negative aerodynamic damping. This is typically termed the floating feedback damping loop. The tower-top velocity ($\dot{x}_{tt}$) is measured and multiplied by a proportional feedback term ($K_{p,TFB}$) which is then combined with the command from the feedback pitch controller

$$\theta_{TFB} = K_{p,TFB} \dot{x}_{tt}, \tag{5a}$$

$$\theta_{FB} = \theta_{FB} + \theta_{TFB}, \tag{5b}$$

where θ_{TFB} is the tower-top feedback pitch command.

4.2 | Feedforward collective pitch controller

The feedforward control approach used a five-beam LIDAR, with four beams focused around the rotor disc and one focused at hub height directly ahead of the turbine, as illustrated in Figure 1.

When using a multiple-beam LIDAR, as in this study, the REWS can be calculated. This was determined by averaging the longitudinal wind speeds at the LIDAR measurement points, which were evenly distributed across the rotor-swept area

$$REWS = \frac{\sum_{i=1}^{n_{beams}} U_{L,i}}{n_{beams}}, \tag{6}$$

where i is the beam number, $U_{L,i}$ is the longitudinal LIDAR-measured wind speed of a beam and n_{beams} is the number of LIDAR beams. The appropriate LIDAR REWS record to be used for the feedforward pitch command had to be recalled at the required time. This required accounting for the transport delay of the wind from the point of measurement to the turbine as well as time delays incurred by filtering. This was achieved through the use of a data storage row vector. Upon each new time step of the simulation, the values stored in the vector were shifted across to vacate the first space of the array for the latest LIDAR REWS measurement. The current LIDAR REWS measurement was then passed through a first-order low-pass filter with the following transfer function:

$$G_{LPF}(s) = \frac{2\pi f_{cut\text{-}off}}{s + 2\pi f_{cut\text{-}off}}, \tag{7}$$

where $f_{cut\text{-}off}$ is the cut-off frequency of the low-pass filter. Details on how this was obtained and the time delay that it incurred are provided in Section 4.5. The gain, G_{LPF}, was applied to filter the LIDAR REWS wind speed measurement, which was then assigned to the first position within the vector.

The approximate lead time (T_{lead}) of the current LIDAR measurement from the point of measurement to the turbine was

$$T_{lead,1} = \frac{\Delta x}{U_{ref}} \tag{8}$$

where Δx is the x-direction focal distance (equal for all beams) and U_{ref} is the reference wind speed. The time within the simulation at which the latest LIDAR wind speed measurement was expected to reach the turbine ($T_{impact,1}$) was

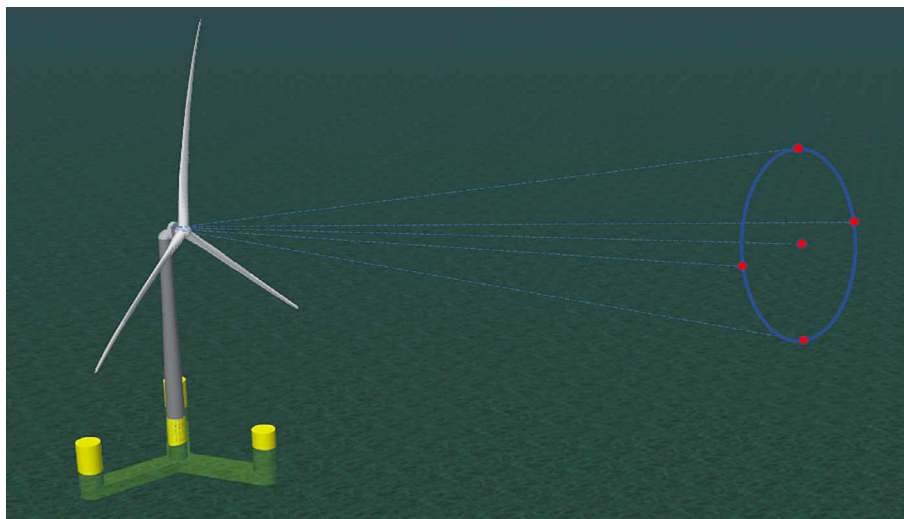$$T_{impact,1} = T_{meas} + T_{lead,1}, \tag{9}$$

FIGURE 1 Illustrating a side view of the nacelle-mounted LIDAR beam trajectories, marked by blue dashed lines, and their focal positions, marked by red dots. Not to scale.

where T_{meas} is the simulation time at the point when the measurement is taken. The impact time was also stored in a data storage row vector housing estimated impact times for each LIDAR REWS record. Similarly to the REWS records, the latest impact time record assumed the first position after the previous records were shifted across. The two data storage vectors were aligned in their positions of the expected time of impact and the filtered LIDAR REWS. The time delays incurred by the first-order low-pass filter of the LIDAR measurements (T_{filter}), the second-order low-pass filter of the pitch actuators (T_{pitch}), the LIDAR full-scan duration, T_{scan} (1 s) and the current simulation time, T, were then subtracted from each of the values in the impact time storage vector, such that values within the vector decreased as T increased. The remaining storage time ($T_{storage,j}$) of data point j at a certain T is defined as

$$T_{storage,j} = T_{impact,j} - T - T_{filter} - T_{pitch} - \frac{1}{2}T_{scan}. \tag{10}$$

The location within the $T_{storage}$ vector that had a value closest to zero was then selected, and the value at the same location within the filtered LIDAR REWS vector was selected as the REWS record to use when calculating the feedforward command for the current time step. The feedforward pitch angle (θ_{FF}) was then determined through interpolation of the wind speed-pitch angle curve, shown in Figure 2.

The difference between θ_{FF} and the feedforward command computed at the previous time step ($\theta_{FF,prev}$) was calculated and divided by the simulation time step duration, Δt, to give the feedforward pitch rate ($\dot{\theta}_{FF}$):

$$\dot{\theta}_{FF} = \frac{\theta_{FF} - \theta_{FF,prev}}{\Delta t}. \tag{11}$$

$\dot{\theta}_{FF}$ was then included within the calculation of I_{FB} (Equation 3):

$$I_{FF\text{-}FB} = I_{FF\text{-}FB,prev} + \Delta t (K_I e_{FB} + \dot{\theta}_{FF}), \tag{12}$$

where I_{FF-FB} is the feedforward modified feedback controller integral component and $I_{FF-FB,prev}$ is the value of I_{FF-FB} computed at the previous time step. The feedforward rate addition methodology has also been applied in previous studies.[1,3,24] P_{FB} (from Equation 2) and I_{FF-FB} were then combined to give the feedforward modified feedback pitch command:

$$\theta_{FF\text{-}FB} = (P_{FB} + I_{FF\text{-}FB}) + \theta_{TFB}. \tag{13}$$

4.3 | Feedback individual pitch controller

The FBIPC approach used in this study, as defined by Bossanyi[13] and Magar et al,[27] used the out-of-plane bending moment at the root of each blade and the rotor azimuth as its feedback inputs. The blade pitch angles are given as a function of the rotor azimuth angle, A, as follows[13]:
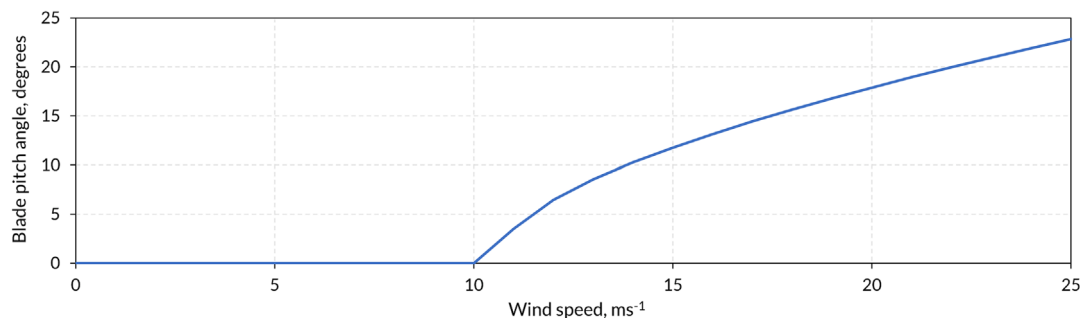
$$\theta_1 = \theta_{avg} \cos(A), \tag{14a}$$

FIGURE 2 Wind speed–blade pitch angle curve.

$$\theta_2 = \theta_{avg} cos\left(A + \frac{2\pi}{3}\right), \tag{14b}$$

$$\theta_3 = \theta_{avg} cos\left(A + \frac{4\pi}{3}\right), \tag{14c}$$

where θ_1, θ_2 and θ_3 are the pitch angles of each blade and θ_{avg} is the mean pitch angle.

The blade pitch angles are then transformed to the d–q axis using a multi-blade coordinate transformation, as was first demonstrated by Bossanyi.[13] This can be applied to convert the three-phase blade root bending moments onto a 2-D perpendicular axis

$$\begin{bmatrix} \theta_d \\ \theta_q \end{bmatrix} = \frac{2}{3} \begin{bmatrix} cos(A) & cos\left(A + \frac{2\pi}{3}\right) & cos\left(A + \frac{4\pi}{3}\right) \\ sin(A) & sin\left(A + \frac{2\pi}{3}\right) & sin\left(A + \frac{4\pi}{3}\right) \end{bmatrix} \begin{bmatrix} \theta_1 \\ \theta_2 \\ \theta_3 \end{bmatrix}, \tag{15}$$

where θ_d and θ_q are the direct and quadrature axis outputs, respectively. The bending moments at the roots of the blades are assumed to be measured and then transformed to d–q axis using Equation (15). The controller is implemented during this transformation to keep the bending moments constant irrespective of changes in them due to variations in the wind speed. An inverse d–q transformation is then performed to convert the control outputs into individual pitch commands:

$$\begin{bmatrix} \theta_1 \\ \theta_2 \\ \theta_3 \end{bmatrix} = \begin{bmatrix} cos(A) & sin(A) \\ cos\left(A + \frac{2\pi}{3}\right) & sin\left(A + \frac{2\pi}{3}\right) \\ cos\left(A + \frac{4\pi}{3}\right) & sin\left(A + \frac{4\pi}{3}\right) \end{bmatrix} \begin{bmatrix} \theta_d \\ \theta_q \end{bmatrix}. \tag{16}$$

The individual pitch command for each blade was then combined with the command from the FFCPC, resulting in

$$\theta_{FF\text{-}FB,k} = (P_{FB} + I_{FF\text{-}FB}) + \theta_{TFB} + \theta_{FB,k}, \tag{17}$$

where $\theta_{FB,k}$ is the FBIPC command for an individual blade, k, and $\theta_{FF\text{-}FB,k}$ is the combined FFCPC + FBIPC pitch command for an individual blade.

4.4 | Feedforward individual pitch controller

In the present study, a novel individual pitch controller was designed to tune each blade's pitch angle depending on its azimuth position. It was used to provide an additional refinement to the feedforward collective pitch controller. The approach used the four outer beams of the five-beam LIDAR illustrated in Figure 1. These were focused at 90° azimuthal increments, as illustrated in Figure 3. Simulations were performed where the beams were positioned at various rotor radial span widths (30%, 50% and 70%) to determine the best-performing beam span positions for the FFCPC + FFIPC. This approach is most similar to that used by Dunne et al,[17,18] though differs in that the LIDAR beams are not rotating with the blades and the collective pitch controller is still used to provide a command to all blades.

Though the beams were focused at the specified points relative to the nacelle, the movement of the nacelle and its impact upon the measurement coordinates and beam azimuth angles were accounted for in real-time. The longitudinal wind speed was recorded at each LIDAR beam's measurement point. These were then individually low-pass filtered using the same cut-off frequencies as were used for the filter on the REWS for FFCPC. The pitch angle associated with the filtered wind speed recorded by each beam, $\theta_{setpoint}$, was then determined through interpolation of the wind speed-pitch angle curve (Figure 2). The azimuth positions of each blade (A_k) at the current time were determined by feedback of the OpenFAST azimuth output (A):

$$A_k = A + \frac{2\pi(k-1)}{3}, \tag{18}$$

where k is the blade number from 1 to 3. The current rotor rotational speed (Ω_r) was then used to predict the azimuth position of each blade ($A_{k,new}$) after the delay incurred by the low-pass filter that will be used on the individual commands (T_{IPC}). An example scenario of this is illustrated
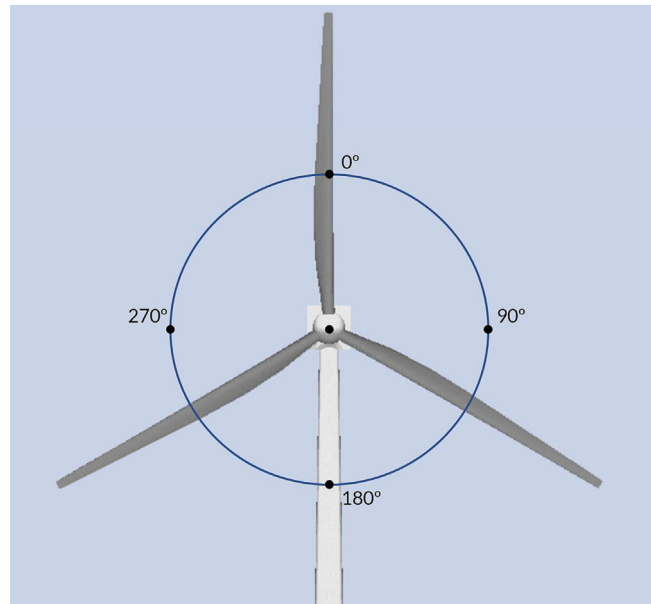
FIGURE 3 Rotor azimuth positions of the LIDAR focal positions within the rotor plane at 50% rotor radial span.

in Figure 4. This assumes that the rotor speed does not change over the delay period incurred by the low-pass filter on the individual pitch commands:

$$A_{k,new} = A_k + \Omega_r T_{IPC}. \tag{19}$$

The expected azimuth angle of each blade was then subtracted from the azimuth angle of each beam (A_i):

$$A_{k,dif} = A_i - A_{k,new}. \tag{20}$$

The beam associated with the smallest difference in azimuth angle ($A_{k,dif}$) was then selected to provide the individual pitch command to the individual blade. The error ($e_{FF,i}$) between the pitch angle setpoint associated with the beam, $\theta_{setpoint,i}$, and the current average blade pitch angle ($\theta_{c,avg}$) was then determined.

$$e_{FF,i} = \theta_{setpoint,i} - \theta_{c,avg}. \tag{21}$$

A low-pass filter with the following transfer function was used to prevent large variations in individual pitch commands:

$$G_{LPF,IPC}(s) = \frac{2\pi f_{cut\text{-}off,IPC}}{s + 2\pi f_{cut\text{-}off,IPC}}, \tag{22}$$

where $f_{cut\text{-}off,IPC}$ is the cut-off frequency of the low-pass filter applied to the feedforward individual pitch commands. Details on how this was determined and the time delay that it incurred are provided in Section 4.5. The gain, $G_{LPF,IPC}$, was applied to filter the feedforward individual pitch commands. This resulted in the feedforward pitch command for the individual blade, $\theta_{FF,k}$. Time series of an individual pitch command pre- and post-filtering are shown in Figure 5.

The time delay incurred by the filter required an additional term, T_{IPC}, to be considered within Equation (10) when accounting for the storage time when undertaking FFIPC such that

$$T_{storage,j} = T_{impact,j} - T - T_{filter} - T_{pitch} - \frac{1}{2}T_{scan} - T_{IPC}. \tag{23}$$
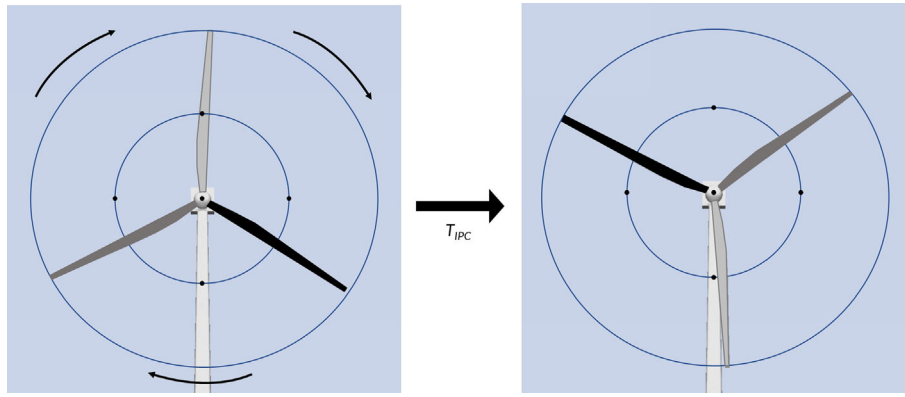
FIGURE 4 Illustrating an example scenario of the rotation of the turbine blades during the time delay incurred by the low-pass filter applied to the feedforward individual pitch commands.
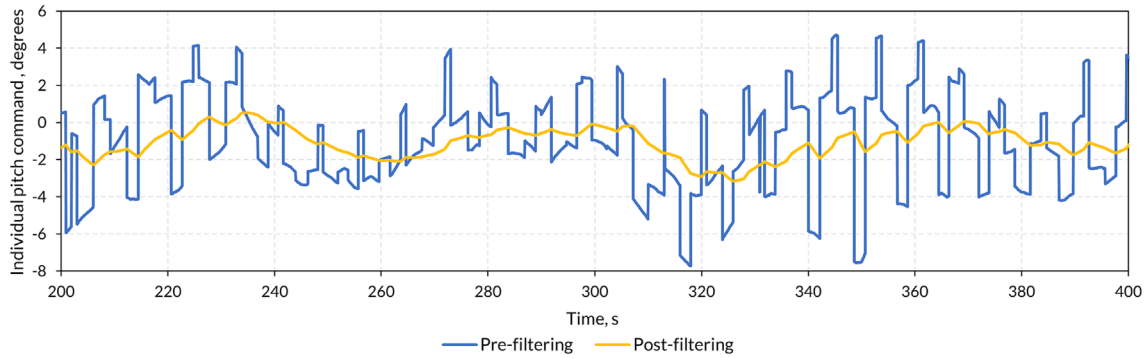

FIGURE 5 Excerpt of time series individual blade pitch commands pre- and post-low-pass filtering.

The individual component of the controller was designed to provide small adjustments to each blade in addition to the collective command that is provided to all of the blades:

$$\theta_{FF\text{-}FB,k} = (P_{FB} + I_{FF\text{-}FB}) + \theta_{TFB} + \theta_{FF,k}. \tag{24}$$

This resulted in an individual pitch variation as shown in Figure 6.

4.5 | Filter design and time delays

This section will outline how the cut-off frequencies and subsequent time delays of the low-pass filters used on the LIDAR REWS measurements, pitch actuators and feedforward individual pitch commands were determined. The time delays determined the minimum x-direction focal distance to ensure that the buffer time, T_{buffer}, in

$$T_{buffer} = T_{lead} - T_{filter} - T_{pitch} - \frac{1}{2}T_{scan} - T_{IPC} \tag{25}$$

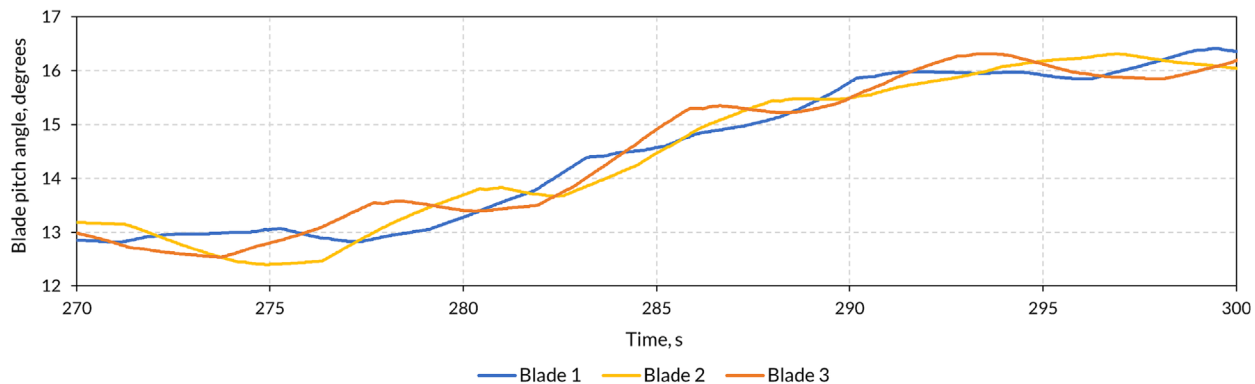was greater than zero at all reference wind speeds.

FIGURE 6   Excerpt of time series individual blade pitch variation when using feedforward individual blade pitch control.

4.5.1 | LIDAR REWS low-pass filter

A low-pass filter was applied to the LIDAR REWS time series measurements to ensure that frequencies above which there was a poor correlation between the LIDAR-measured REWS and the REWS experienced by the turbine were not considered. This point was defined by the cut-off frequency of the filter. Without filtering, or with the cut-off frequency set too high, uncorrelated frequencies would be used by the LIDAR-assisted controller, leading to incorrect control action. The cut-off frequency was determined through analysis of the transfer function between time series of the LIDAR-measured and turbine REWS, $|G_{RL}|$. $|G_{RL}|$ takes a value between 0 and 1 and indicates the quality of LIDAR preview.[24,28]

$$|G_{RL}(f)| = \frac{|S_{RL}(f)|}{S_{LL}(f)}, \tag{26}$$

where S_{LL} is the auto-spectrum of the LIDAR and estimated REWS and S_{RL} is the cross-spectrum of the LIDAR and turbine REWS estimates. This transfer function can also be derived theoretically if the turbulence spectra and coherence are known. From time series measurements, the spectra were calculated over a 10-min period. The resulting frequency domain (f) was converted into the wavenumber domain (k) using Taylor's frozen turbulence hypothesis[29]:

$$k = \frac{2\pi f}{U_{ref}}. \tag{27}$$

To compare to the LIDAR REWS measurements, the turbine-based REWS was determined by extracting outputs from multiple nodes within OpenFAST, discretized to 10-m increments across the rotor-swept area. These were then averaged to determine the REWS. S_{RL} and S_{LL} were determined using MATLAB's cross power spectral density (PSD)[30] and Welch's PSD estimate[31] functions, respectively. The spectra can also be determined analytically and details of this are provided within the literature.[28,29] The LIDAR and turbine REWS time series used in the analysis are shown in Figure 7. These resulted in a transfer function spectrum as shown in Figure 8.

The wavenumber at which $|G_{RL}|$ reaches $-3\,\text{dB} \approx 0.7$ is termed the maximum coherent wavenumber, $\hat{k}$. From Figure 8, this occurred at a wavenumber of $0.01563\,\text{rad}\,\text{m}^{-1}$. This process was repeated for beams positioned at 30% and 70% radial span, yielding a $\hat{k}$ of 0.0070 and $0.0208\,\text{rad}\,\text{m}^{-1}$, respectively. The cut-off frequencies for different reference wind speeds for each LIDAR beam configuration were then determined.[28]

$$f_{cut\text{-}off} = \frac{\hat{k}U_{ref}}{2\pi}. \tag{28}$$

Figure 9 shows the value of $f_{cut\text{-}off}$ at different reference wind speeds for the different beam configurations.

The low-pass filter for the REWS is first order and incurs a time delay (T_{filter}), which can be approximated at a certain frequency $\omega_{delay} = 2\pi f_{delay}$, $\omega_{cut\text{-}off} = 2\pi f_{cut\text{-}off}$ using equations from Schlipf[28]:
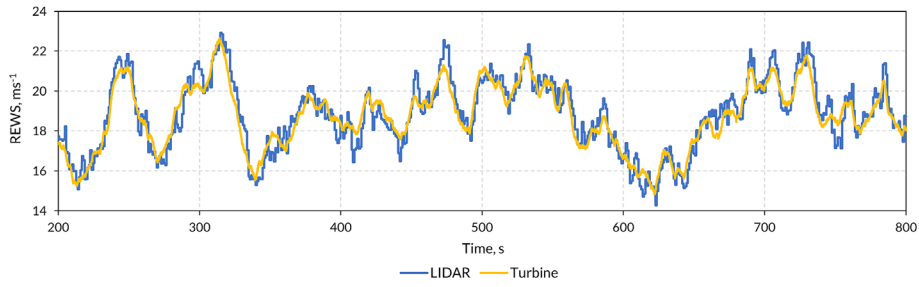
FIGURE 7 Ten-minute time series of LIDAR (radial span = 50%) and turbine-based REWSs used in the coherence analysis.
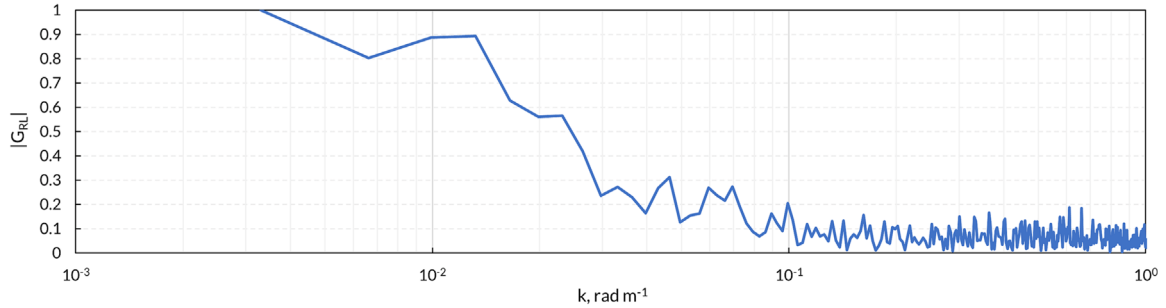

FIGURE 8 Transfer function between the LIDAR (radial span = 50%) and turbine REWS simulation data as a function of wave number.
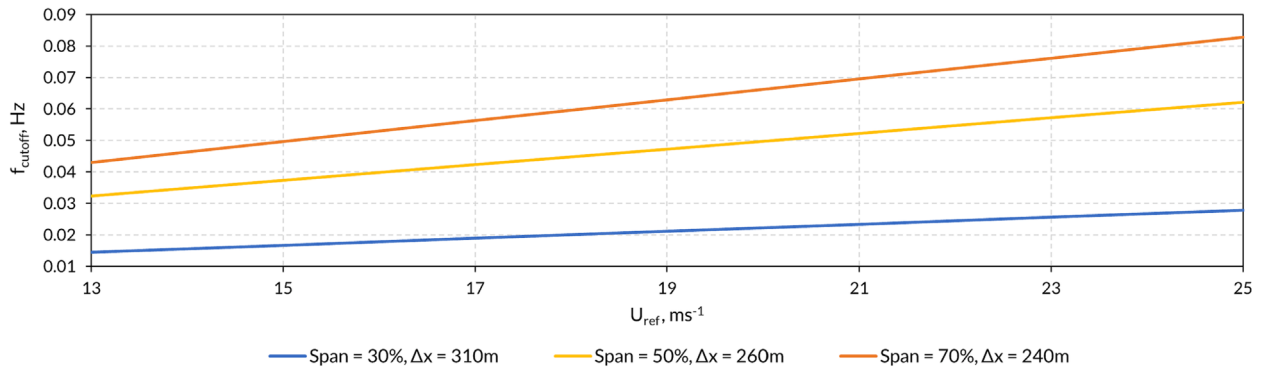

FIGURE 9 $f_{cut\text{-}off}$ at different average wind speeds for each of the radial span locations at their minimum x-direction focal distances.

$$T_{filter} = \frac{arctan(\omega_n)}{\omega_{delay}} \, with \, \omega_n = \frac{\omega_{delay}}{\omega_{cut\text{-}off}}. \tag{29}$$

The pitch actuator uses a second-order low-pass filter, whose time delay can be approximated using[28]

$$T_{pitch} = \frac{arctan\left(\frac{\sqrt{2}\omega_n}{1-\omega_n^2}\right)}{\omega_{delay}}. \tag{30}$$

In both Equations (29) and (30), f_{delay} was set to 0.025 Hz, as this is the critical frequency near where the IEA 15 MW turbine's rotor has higher fluctuations.[12]

4.5.2 | FFIPC low-pass filter

As discussed in Section 4.4, a low-pass filter was required to smoothen and reduce the magnitude of the feedforward individual pitch commands. To achieve this, the cut-off frequency had to be set to a low level, which also mitigated interference with key turbine and substructure frequencies. In this work, $f_{cut-off}$ of the FFIPC filter was set to 0.0132 Hz, which is below the platform pitch rigid-body natural frequency (0.036 Hz[10]) as well as the frequency where the turbine's rotor has higher fluctuations (0.025 Hz[12]). There was not expected to be interference with the tower frequencies because, for this FOWT, the tower first natural frequencies were above the 3P range, as was explained in Section 2.1.3. Consequently, this filter resulted in an additional time delay (T_{IPC}) to be subtracted from T_{lead} in Equation (25), calculated using Equation (29). This resulted in the requirement for higher values of T_{lead} to ensure that T_{buffer} was greater than 0 at all wind speeds, as shown in Figure 10. This was achieved by setting the x-direction focal distance of the beams to 310, 260 and 240 m for beams focused at 30%, 50% and 70% radial span, respectively. The minimum x-direction focal distance decreased as the radial span increased because values of $\hat{k}$ and, therefore, $f_{cut-off}$ (Figure 9) were greater as the radial span increased. Higher values of $f_{cut-off}$ result in lesser time delays incurred by the low-pass filter on the LIDAR REWS. Therefore, less lead time was required and the LIDAR beams could be focused at positions closer to the turbine.

5 | SIMULATIONS

Turbulent wind fields were created using TurbSim,[32] with average wind speeds covering the above-rated wind spectrum, from 13 to 25 ms^{-1} in intervals of 2 ms^{-1}. These were generated for four random seeds of 1-h length (3800 s were simulated but the first 200 s were discarded to remove start-up transients) to provide a variety of turbulent wind profiles. Although the authors are aware of the challenges brought by the transition between the above- and below-rated control regions,[33] the behaviour of the controllers around this transition is not explicitly examined in this work. The turbulence was generated under the normal turbulence model (NTM), turbulence intensity (TI) Category B.[32] These conditions fall into design load case (DLC) 1.2, as defined in the IEC standards.[34] DLC 1.2 was used as this embodies the loads resulting from turbulence that occurs during the normal operation of a wind turbine throughout its lifetime. The FOWT was modelled in a water depth of 200 m and under irregular waves. The wind and waves were aligned in the same direction. The significant wave height (H_s) and peak spectral period (T_p) were adjusted to suit each average wind speed integer, with values interpolated from those defined by Allen et al,[10] and shown in Table 3.

5.1 | Statistical metrics

The benefits of LIDAR-assisted control can be assessed by statistical metrics, the choice of which varies depending on the desired outcome most relevant to the parameter. The metric most commonly used when assessing the performance of LIDAR-assisted control is the standard deviation,
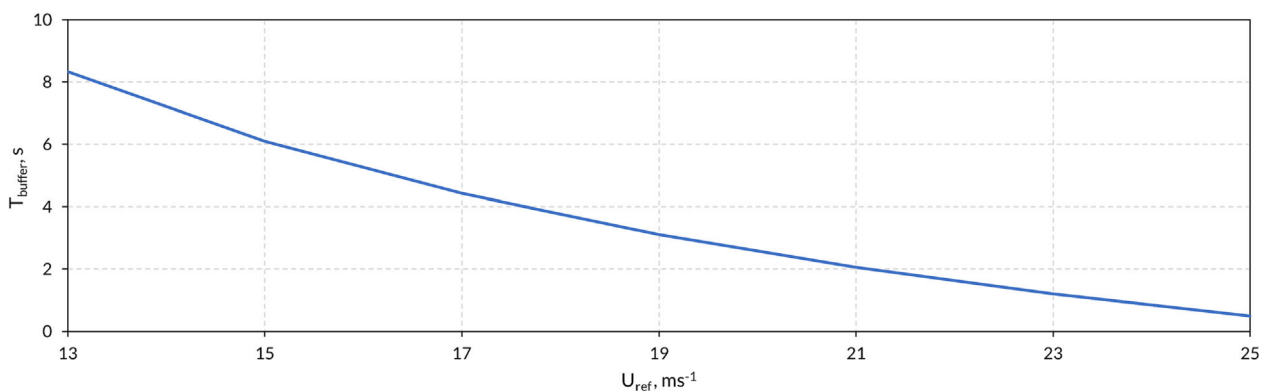

FIGURE 10 T_{buffer} at different reference wind speeds for beams positioned at 50% radial span at an x-direction focal distance of 260 m.

TABLE 3 IEC DLC 1.2 NTM wind and wave conditions.[10]

U_{hub} (ms^{-1})	13	15	17	19	21	23	25
H_s (m)	2.0	2.4	2.8	3.3	3.8	4.3	4.8
T_p (s)	7.5	7.6	7.8	8.3	8.8	9.2	9.7

TABLE 4 Detailing the key performance indicating metrics that were assessed for the specified parameter and their significance in demonstrating the efficacy of LIDAR-assisted control.

Parameter	Metric	Significance
Rotor speed	RMSE	This metric can assess how closely the rotor speed is maintained at its rated value (7.56 rpm). A lower error therefore indicates that the pitch controller is better able to deliver its control objective.
	Range	The range in rotor speed determines the 1P and 3P ranges, which are important for substructure and tower design. Allen et al[10] reported that, for the IEA 15 MW reference turbine on the VolturnUS-S, the constraining operational rotor speed range was 3.97 to 8.86 rpm, which impacted upon the tower design. Reductions to the 1P and 3P frequency ranges may allow for the use of a soft-stiff tower, which will be a lighter and cheaper option than a stiff-stiff tower.
	Maximum	Floating wind turbines are prone to over-speeding by up to 30% greater than the rated rotor speed,[4,6] which can lead to shutdowns and damage to turbine components.
Power	RMSE	This metric can assess how closely the generator power is maintained at its rated value (15 MW). Significant variation around the setpoint can lead to excessive stress on the generator.
Blade pitch	σ	Decreased standard deviations indicate a reduced degree of pitch actuation and, therefore, less demand on the pitch actuation mechanisms.
	Rate	This metric provides information on how quickly the blade pitch angle changes between measurements and can provide further indication of the demand on the pitch actuation mechanisms.
Thrust	σ	A reduced standard deviation in the thrust indicates a reduction in the variation on the force applied to the wind turbine.
Bending moments	σ	Reductions indicate that the loadings are more consistent, predictable and uniform across the structure and can result in reduced fatigue, failure rates and, therefore, lifetime extension.
	DEL	Similarly to σ, lower DELs indicate reduced stress on turbine components and structures, which can result in reduced fatigue and, ultimately, lifetime extension and cost savings.
Platform motions	σ	Reductions to the standard deviation indicate reduced magnitude and variation of platform motions, which can improve stability and lead to performance improvements.
	Acceleration (pitch only)	Access to the turbines can be limited by the acceleration of the platform motions, primarily in pitch and, therefore, it is favourable to reduce them.
	Maximum (pitch only)	The maximum magnitude of platform motions, particularly the platform pitch angle, is a design constraint for the turbine–substructure design as it plays a role in dictating the aerodynamic efficiency and the loads at the tower base.

σ, which provides knowledge of the degree of variation within the data set. The root mean squared error (RMSE) metric can be applied to assess the ability of the controller to maintain the control variables (viz., the rotor speed and power) at their desired set points. For bending moments, the damage equivalent loads (DELs) can also be compared. DELs equate to the load experienced by the turbine structure/component over a period of time that is equivalent to the damage caused by a specific event. The other metrics used to compare the time series results of the controllers were the ranges, maximum values, rates of change and accelerations. Table 4 highlights the key performance indicating metrics that were assessed for the various turbine and substructure parameters, with rationale explaining their significance.

6 | RESULTS AND DISCUSSION

This section presents the results of the OpenFAST simulations for the single turbine. Results are presented as normalized values, whereby the values were divided by that of the feedback-only controller.

$$X_{i,normalized} = \frac{X_i}{X_{FB}}, \tag{31}$$

where X_i is the value of a metric for a given parameter associated with a control strategy, i (FB, FFCPC, FFCPC + FBIPC or FFCPC + FFIPC), and $X_{i,normalized}$ is the normalized value of a metric for a given control strategy. This approach allows for direct comparison to the results of the feedback controller, which are normalized to 1. Therefore, a value that is less than one indicates a reduction (and therefore an improvement) compared to the baseline feedback controller and a value that is greater than one indicates an increase (and therefore a deterioration) compared to the baseline feedback controller.

6.1 | Feedback versus feedforward control

This section outlines the results of the simulations. Time series results of a single seed with an average wind speed of 17 ms^{-1} will be first shown, to highlight the improvements to the turbine and substructure parameters when using the FFCPC or FFCPC + FFIPC compared to the feedback-only controller. Results of the FFCPC + FBIPC will also be presented to compare the effectiveness of the feedback and feedforward individual control elements. Four seed average results from across the above-rated spectrum will then be given to further demonstrate the capability of the feedforward controllers.

6.1.1 | Single wind field

Figure 11 presents an excerpt of time series results of the selected turbine and substructure parameters.

Table 5 provides a summary of the averaged normalized metric values for various parameters delivered by the feedforward control strategies relative to the baseline feedback controller across four random seed 1-h length simulations.

As can be seen from Figure 11 and Table 5, the collective and individual pitch control additions are able to deliver benefits to the key metrics of numerous turbine and substructure parameters. The rotor speed and generator power benefitted most significantly, with reductions of up to 54% in the RMSEs compared to the baseline feedback controller, demonstrating improved power tracking, and reduced ranges of 1P and 3P
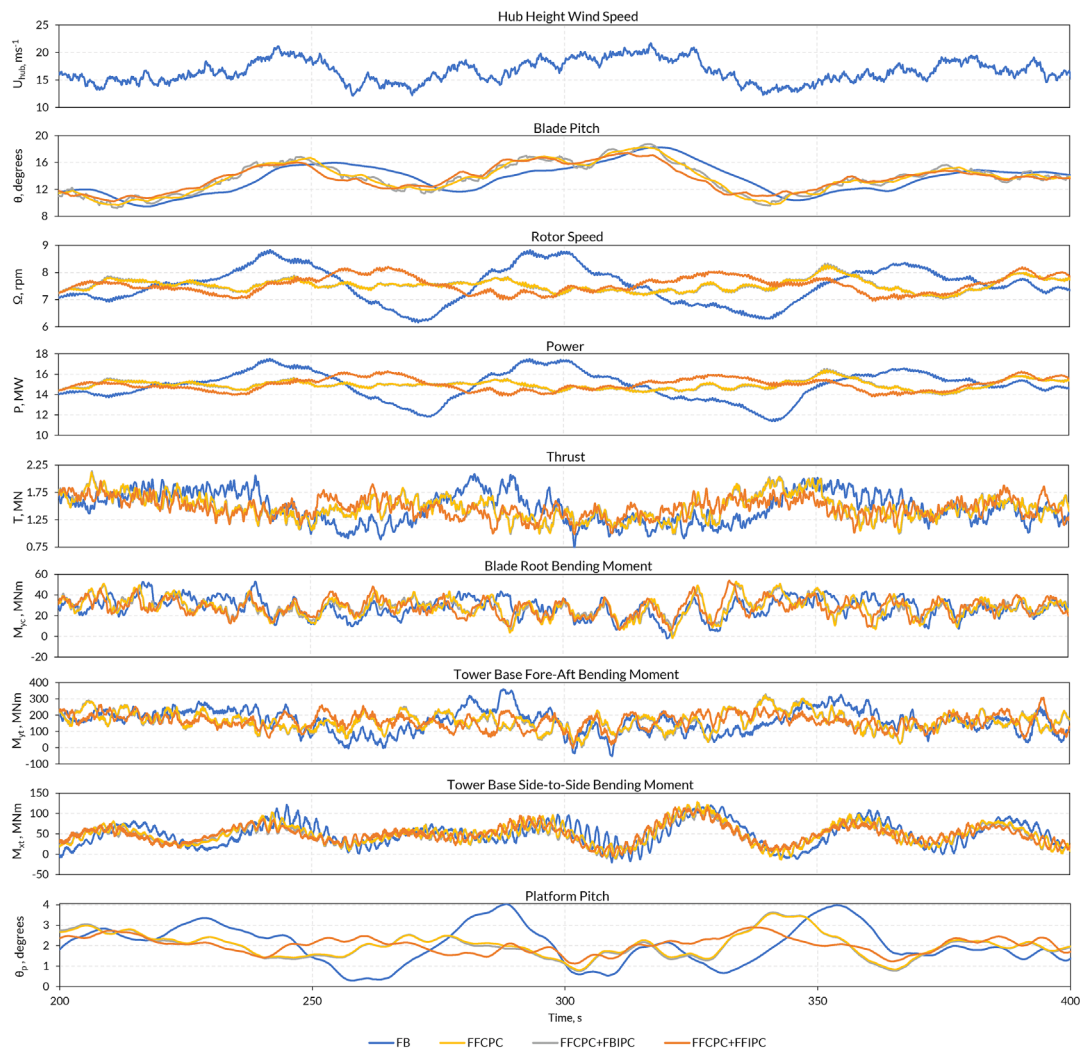

FIGURE 11 Two hundred-second excerpt time series results comparing the baseline FB pitch controller to the FF controllers. Simulations were performed under a turbulent wind field ($U_{avg} = 17$ ms^{-1}, NTM, TI Category B) and irregular waves ($H_s = 2.83$ m, $T_p = 7.85$ s). The LIDAR beams were positioned at 50% rotor radial span for all feedforward control strategies.

TABLE 5 Normalized metric values of various parameters through the addition of feedforward pitch control versus baseline feedback control under a turbulent wind field ($U_{avg} = 17\,\text{ms}^{-1}$, NTM, TI Category B) with irregular waves ($H_s = 2.83\,\text{m}$, $T_p = 7.85\,\text{s}$).

Parameter	Metric	Normalized FB	Normalized FFCPC	Normalized FFCPC + FBIPC	Normalized FFCPC + FFIPC
Performance					
Rotor speed	RMSE	1.00	0.48	0.47	0.48
	Range	1.00	0.54	0.54	0.56
	Maximum	1.00	0.93	0.93	0.92
Power	RMSE	1.00	0.47	0.46	0.46
Blade pitch	σ	1.00	1.02	1.03	0.95
	Rate	1.00	1.44	4.62	1.48
Thrust	σ	1.00	0.86	0.86	0.78
Bending moments					
Blade root	σ	1.00	0.97	0.89	0.94
	DEL	1.00	1.00	0.93	0.96
Tower base fore–aft	σ	1.00	0.85	0.85	0.80
	DEL	1.00	0.91	0.92	0.89
Tower base side-to-side	σ	1.00	1.00	0.96	1.02
	DEL	1.00	0.98	0.96	1.00
Platform motions					
Pitch	σ	1.00	0.74	0.73	0.64
	Acceleration	1.00	0.83	0.83	0.78
	Maximum	1.00	0.90	0.89	0.82
Roll	σ	1.00	1.01	0.96	1.03
Yaw	σ	1.00	1.01	0.79	0.94
Heave	σ	1.00	1.02	1.02	1.02
Surge	σ	1.00	0.88	0.88	0.76
Sway	σ	1.00	1.01	0.85	1.05

Note: The LIDAR beams were positioned at 50% rotor radial span for all feedforward control strategies. Results shown are average normalized values across the four random seed 1-h simulations at $U_{avg} = 17\,\text{ms}^{-1}$.

frequencies by up to 46%. These benefits are attributed to the superior blade pitch preparation in advance of the wind's impact. This has a damping effect on the rotor's motion, thereby reducing its variation compared to the feedback-only controller. However, to achieve this, the average rate of change of the blade pitch was increased, especially when using FFCPC + FBIPC, which indicates an increased demand on the pitch actuation mechanisms. Despite the increases to the pitch rate, the average deviation of the blade pitch angle from its mean value was not affected significantly and was slightly reduced when FFCPC + FFIPC was employed. The standard deviations of the bending moments on the blade roots and tower were reduced by up to 20%, which led to reductions in DELs by up to 11% compared to the baseline feedback controller. The variation in the blade root loads were reduced most when combining the feedforward CPC with the traditional FBIPC (FFCPC + FBIPC) because maintaining the blade root bending moments as constant is a control objective of this approach, as was explained in Section 4.3. In terms of platform motions, the greatest beneficiary was the pitch degree of freedom, where 26% and 36% reductions in the standard deviation compared to the baseline were recorded for FFCPC and FFCPC + FFIPC, respectively. This was expected because the thrust force reported its greatest reduction in standard deviation with FFCPC + FFIPC, meaning that a more consistent force was applied to the rotor when using feedforward control instead of feedback-only control, resulting in reduced variation in the force pushing the turbine backwards. This led to the reduced variations seen in the pitching of the platform as well as the fore–aft bending moment acting on the tower base.

Overall, the FFCPC + FFIPC strategy further enhanced the FFCPC by providing additional tuning to the pitch of the individual blades. Performance parameters benefitted from up to 8% further reductions in the standard deviation compared to the baseline feedback controller, though the benefits to the rotor speed and power were not enhanced further. The blade root and tower base fore–aft bending moments benefitted from further 3% and 5% reductions in their standard deviations compared to the baseline, respectively. The most significant improvement delivered by FFCPC + FFIPC to the platform's motions was in surge, which achieved a further 12% reduction in standard deviation compared to the baseline feedback controller, while the platform pitch observed a 10% further reduction in its standard deviation and 5% and 8% further reductions to its acceleration and maxima, respectively.

The FFCPC + FFIPC strategy was able to offer improvements upon the traditional FBIPC strategy, though both excelled in different areas. When combined with FFCPC, FFIPC gave greater improvements to the rotor thrust than when FBIPC was used, while also greatly benefiting the platform pitch and surge motions in addition to the tower base fore–aft bending moment. These benefits were also achieved without large increases to the blade pitching rate, as were observed with the FBIPC. However, FBIPC was able to offer benefits over the FFIPC to the blade root and tower side-to-side bending moment as well as the yaw and sway motions of the platform.

The improvements offered by the FFCPC + FFIPC strategy over the baseline feedback control can also be illustrated by PSD plots. Figure 12 presents PSD plots for the rotor speed, blade pitch, platform pitch and tower base fore–aft bending moment. The sampling frequency used in the simulations was 40 Hz, and this is the maximum frequency value of the plots shown in Figure 12.

The rotor speed, platform pitch and tower base fore–aft bending moment's spectra were reduced in the frequency range below the 1P range at 0.2 Hz, indicating a reduction in the influence of the wind disturbance, as was expected, and was consistent with the findings shown in Figure 11 and Table 5. Above this frequency, the spectra for the rotor speed and tower base fore–aft bending moment when using FFCPC + FFIPC were very similar to those of the baseline controller because the feedforward pitch commands were damped out by the low-pass filter. The spectrum of the blade pitch for FFCPC + FFIPC was greater than that of the baseline between the 1P and 3P ranges, which was also expected due to the increase to the average pitch rate.

6.1.2 | Above-rated wind spectrum

Simulations were performed across the above-rated wind spectrum from 13 to 25 ms^{-1} in intervals of 2 ms^{-1}. This aimed to capture the performance benefits attainable from FFCPC with FBIPC or FFIPC across the full operating range of the pitch controller to allow for the assessment of lifetime benefits. The four seed average wind speed series results for various turbine and substructure parameters are shown in Figure 13.

Figure 13 re-iterates the enhancements to FFCPC provided by the FFIPC and FBIPC controllers, as these were able to deliver greater standard deviation reductions for the majority of the above-rated wind speeds. In general, the improvements delivered by the feedforward controllers to the turbine and substructure parameters were least significant at lower above-rated average wind speeds closer to the above–below-rated
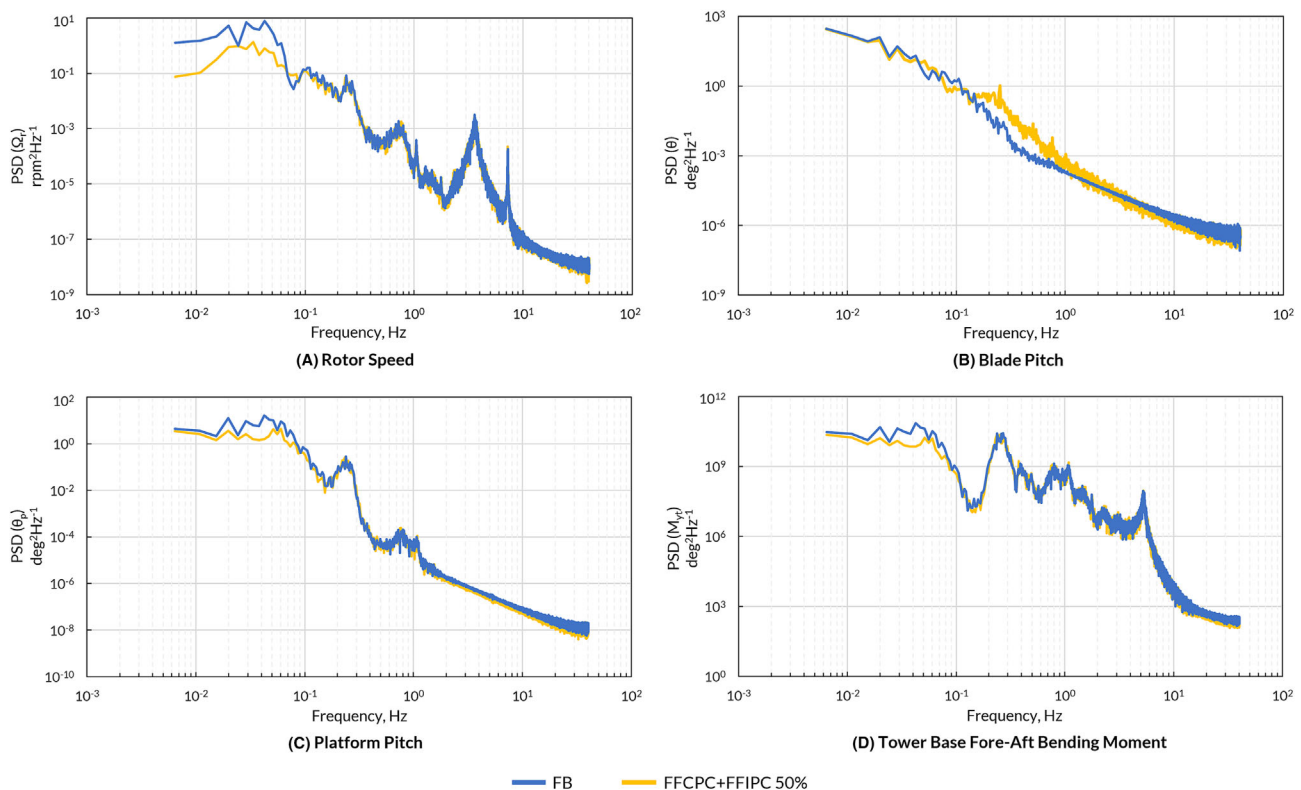

FIGURE 12 PSD plots of the rotor speed, blade pitch, platform pitch and tower base fore–aft bending moment generated from 1 h simulations with a turbulent wind field ($U_{avg} = 17$ ms^{-1}, NTM, TI Category B) and irregular waves ($H_s = 2.83$ m, $T_p = 7.85$ s). The LIDAR beams were positioned at 50% rotor radial span for the FFCPC + FFIPC control strategy.
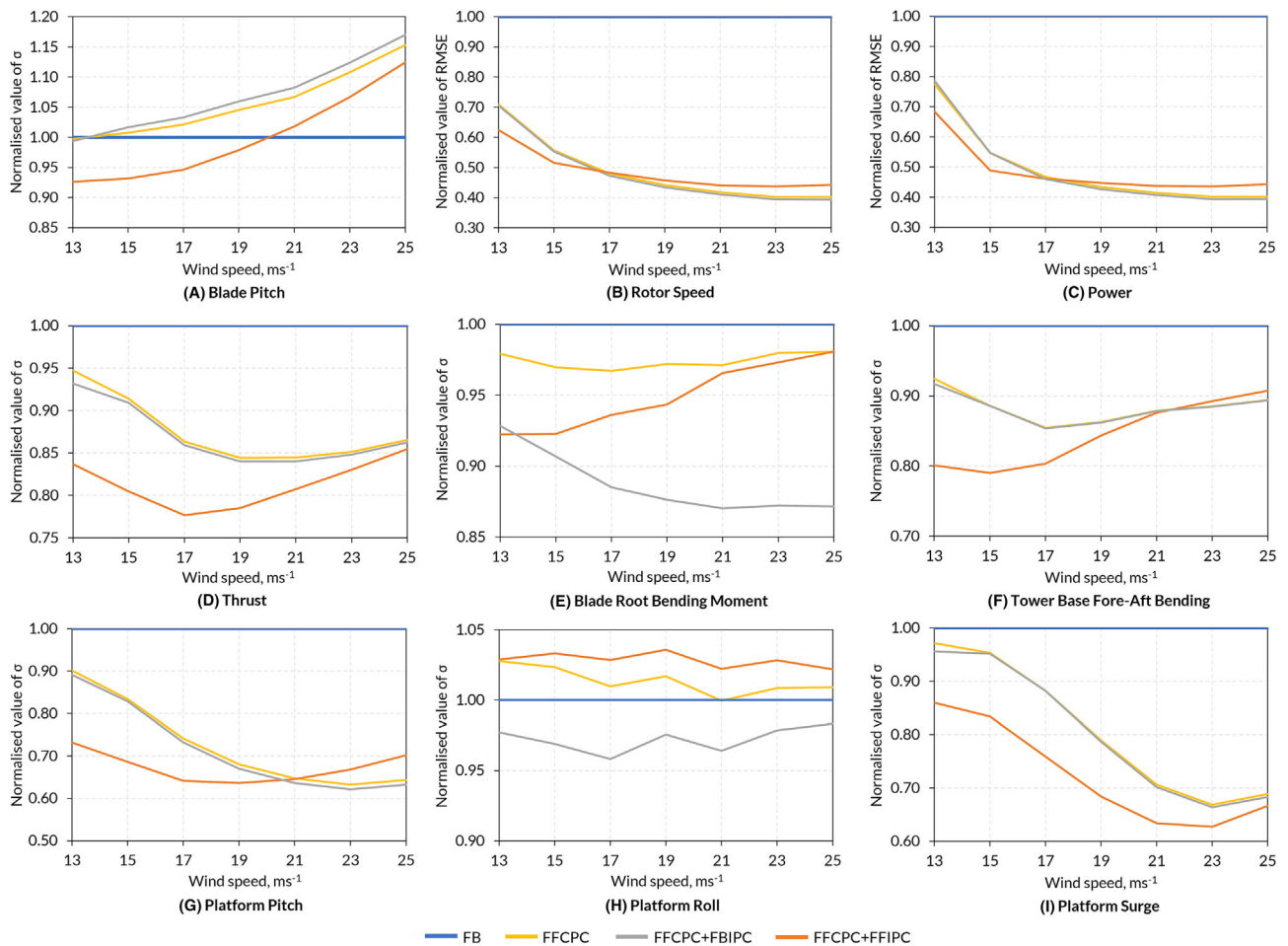
FIGURE 13 Normalized σ or RMSE values delivered by the feedforward controllers compared to the baseline FB-only pitch controller across the above-rated wind spectrum. The LIDAR beams were positioned at 50% rotor radial span for all feedforward control strategies. The results shown are the four seed average normalized values from the 1-h simulations at each average wind speed integer for each control configuration.

transition point (13 and 15 ms^{-1}). This is because, as these are average wind speeds, part of the simulations are spent with wind speeds below the rated speed where the feedforward controllers do not operate, meaning that responses were identical to the feedback-only controller, thereby reducing the differences between the datasets.

As the wind speeds increased, some parameters experienced greater variation and higher magnitude oscillations when using the baseline feedback controller and so this led to more room for improvement for the feedforward controllers. This was true for the rotor speed (Figure 13B) and power (Figure 13C), which benefitted most significantly, with reductions in their RMSEs by up to 60% at an average wind speed of 25 ms^{-1}. This came at the expense of increased variation in the blade pitch as the wind speed increased, by up to 17% greater than the baseline at an average wind speed of 25 ms^{-1}, though FFCPC + FFIPC was able to reduce this increase. The rotor thrust (Figure 13D) saw reductions in the standard deviation delivered by the feedforward controllers increase until approximately 17–19 ms^{-1} before decreasing at higher wind speeds due to diminishing variation in the rotor thrust as the wind speed increased. This was mirrored within the loadings and platform motions, as reductions to the standard deviations of the tower base fore–aft bending moment (Figure 13F), platform pitch (Figure 13G) and platform surge (Figure 13I) also diminished at higher wind speeds due to the decreased reduction to the standard deviation of the rotor thrust. The benefit to the blade root bending moment (Figure 13E) remained relatively consistent across the full above-rated wind spectrum when using FFCPC, though greater improvements were observed when pairing FFCPC with FBIPC, as maintaining the blade root bending moments constant is a control objective of this approach, as was explained in Section 4.3.

6.2 | Comparison of beam span locations

Figure 14 shows the above-rated wind spectra results of the simulations when using beams focused at 30%, 50% and 70% rotor radial span.
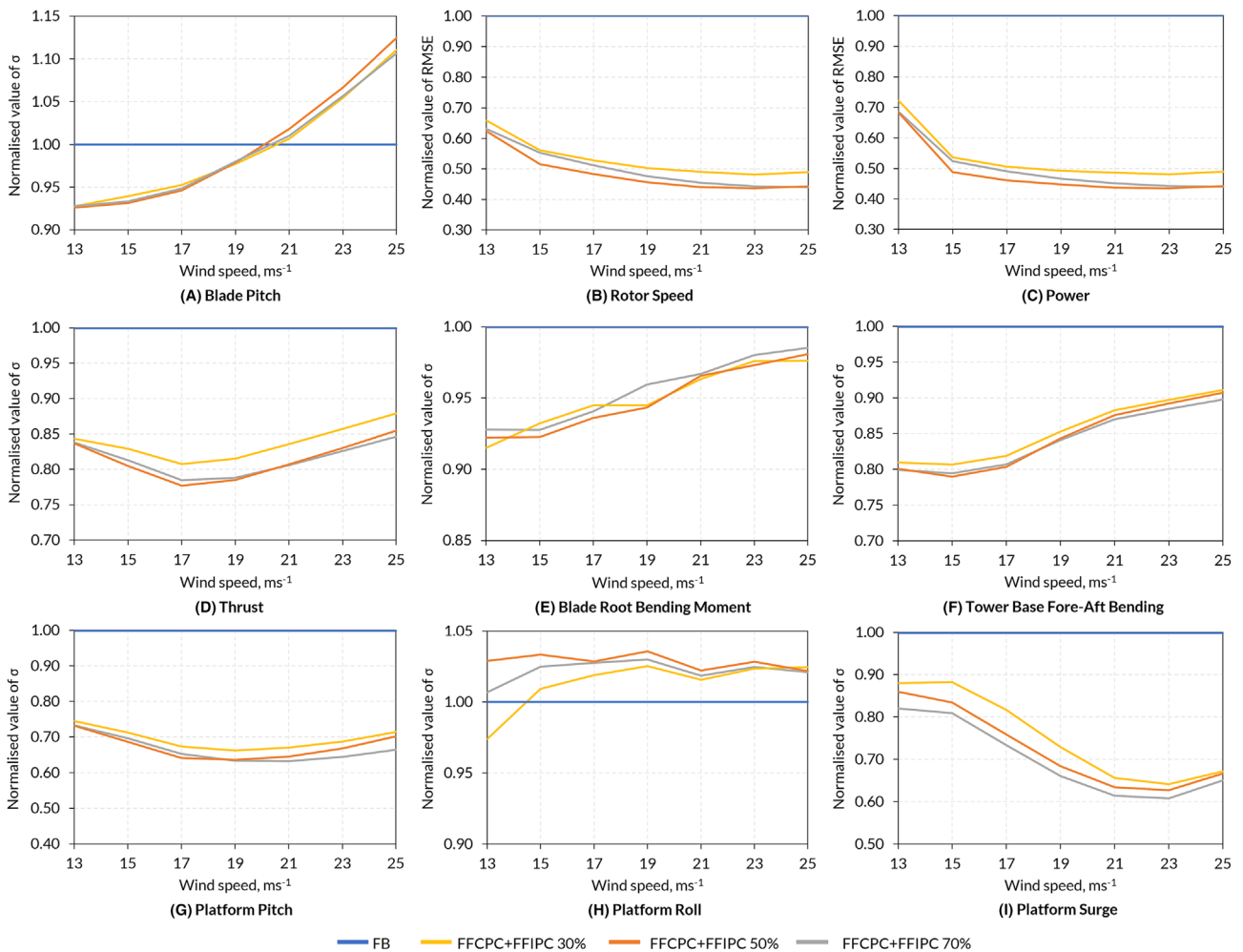
FIGURE 14 Normalized σ or RMSE values delivered by the FFCPC + FFIPC controller with beams positioned at 30%, 50% and 70% rotor radial span compared to the baseline feedback pitch controller across the above-rated wind spectrum. The results shown are the four seed average normalized values from the 1-h simulations at each average wind speed integer for each control configuration.

From Figure 14, the FFCPC + FFIPC performed marginally better across the above-rated wind spectrum when the beams were focused at 50% or 70% than at 30% span. At 30% span, the benefits to the rotor speed (Figure 14A), power (Figure 14B), rotor thrust (Figure 14D) and platform pitch (Figure 14G) were all slightly less significant. The FFCPC + FFIPC performed similarly with beams positioned at 50% and 70% span. However, there were marginally greater benefits delivered when the beams were focused at 50% span compared to at 70% span, namely, in the rotor speed (Figure 14B), power (Figure 14C) and blade root bending moment (Figure 14E), by up to 4%.

The differences seen in the performance of the feedforward IPC at various rotor radial spans can be explained through consideration of the variation in the wind speed across the rotor-swept area as the span positions increase. At 70% span, the distance between the opposite beams was approximately 170 m, compared to 120 m at 50% span and 75 m at 30% span. As a single average wind speed was used by the feedforward collective pitch controller, the potentially larger differences in wind speed at the measurement locations impact upon the REWS used and so may lead to sub-optimal commands issued by the feedforward CPC. Similarly, at the smallest span length simulated (30%), the variation in the measured wind velocities may not be sufficient to represent the full rotor-swept area. This was evidenced by the lower coherence between the LIDAR-estimated and turbine-based REWS, meaning that lower cut-off frequencies were required within the low-pass filter, limiting the feedforward control action. Furthermore, for the individual control element, it is pertinent to capture the variation across the rotor-swept area in order to provide the appropriate command to the individual blades. Therefore, with the beams positioned at 50% rotor radial span, the LIDAR was able to capture the wind velocities appropriate for the effective operation of both the collective and individual feedforward pitch control elements.

6.3 | Study limitations

As was discussed in Section 3.1, the wind velocity is assumed to not evolve from the point of measurement to the turbine (therefore assuming Taylor's frozen hypothesis), 100% LIDAR measurement availability has been assumed and the impact of blade blockage of the LIDAR beams has not been considered. Moreover, the impacts of the velocities, accelerations and rotations of the LIDAR device were not accounted for. The assumptions made may have resulted in an overestimation of the LIDAR preview quality, which will be investigated in future work. Therefore, it is recommended that the results presented in this study be considered as the best-case scenario of what can be achieved through the implementation of the detailed LIDAR-assisted controllers used within this work. Furthermore, the simulations were only performed under normal operating conditions (DLC 1.2). Therefore, the scope of this study does not account for extreme operating conditions and gusts.

7 | CONCLUSIONS

This study has presented a novel LIDAR-assisted FFIPC approach in combination with a feedforward CPC strategy. This was applied to the IEA-Wind 15 MW reference wind turbine mounted on the UMaine VolturnUS-S semi-submersible floating substructure. The benefits of the feedforward IPC were investigated using modified versions of OpenFAST and ROSCO. LIDAR simulation was added to the OpenFAST program through modification to the source code of the InflowWind module. The changes made are now present in the latest release of OpenFAST, v3.5. LIDAR measurements were then interfaced to ServoDyn to allow for transfer to ROSCO for LIDAR-assisted control, where code for collective and individual feedforward pitch control was incorporated. The results presented demonstrate the efficacy of the LIDAR simulation and control additions to OpenFAST and ROSCO and can serve as a demonstration of the capabilities of the LIDAR simulation available in OpenFAST v3.5.

Simulations were performed on a single floating turbine, which yielded significant time series standard deviation, RMSE, range and maxima reductions for both collective and individual feedforward controllers over the baseline feedback collective and individual controllers. The individual feedforward pitch controller was able to provide enhancement to the collective feedforward pitch controller through increased standard deviation reductions over the baseline feedback controller by up to 12% (recorded in the platform surge motion) at an average wind speed of 17 ms^{-1}. Simulations were performed to cover the full above-rated wind spectrum. For some parameters, the standard deviation and RMSE reductions delivered by the feedforward controllers increased with increasing wind speed, while for others, the reductions increased up to an average wind speed of 19 ms^{-1} before diminishing at higher average wind speeds. The feedforward collective combined with the feedforward individual controller was found to give the greatest benefits over the baseline feedback controller, primarily in the rotor thrust, platform pitch, platform surge and tower base fore–aft bending moment, due to the wind speed-azimuth focused tuning of the blade pitch. The combined feedforward collective and individual pitch controller was studied at multiple rotor radial percentage span locations. The controller was found to perform best when the beams were focused at 50% span, offering the best balance between the rotor-effective average wind speed used by the collective control element while capturing the variation across the rotor-swept area used for the individual control component.

Future work aims to investigate the potential degree of overestimation in the LIDAR preview quality obtained from the detailed LIDAR simulator through comparison with an alternative simulator. Lifetime operations and maintenance cost reductions of floating offshore wind turbines will also be quantified through assessment of the lifetime failure rate and DEL reductions. Further work will also aim to investigate the potential for structural optimization of the tower given the LIDAR-assisted controller's ability to reduce the range in the rotor speed and therefore the 1P and 3P frequency ranges.

AUTHOR CONTRIBUTIONS
Andrew J. Russell conceived the concept, performed the modifications to the OpenFAST and ROSCO source codes, executed the simulations and prepared the paper. Maurizio Collu, Alasdair S. McDonald, Philipp R. Thies, Aidan Keane and Alexander R. Quayle provided supervision and suggestions and reviewed the paper.

CONFLICT OF INTEREST STATEMENT
The authors declare no potential conflict of interest.

PEER REVIEW
The peer review history for this article is available at https://www.webofscience.com/api/gateway/wos/peer-review/10.1002/we.2891.

DATA AVAILABILITY STATEMENT

The original modified version of OpenFAST v.3.4, which includes the LIDAR simulator used in this work can be accessed via https://github.com/Russell9798/OpenFAST-v3.4-Lidar-IfW-Original/releases/tag/2.0. The modified version of ROSCO v2.6 with the feedforward control additions can be accessed via https://github.com/Russell9798/ROSCO-v2.6-LAC-IPC/releases/tag/2.0. Simulation datasets used for this paper are available and can be assessed via https://doi.org/10.17605/OSF.IO/FE6YP.

ORCID

Andrew J. Russell https://orcid.org/0009-0008-2534-7664
Maurizio Collu https://orcid.org/0000-0001-7692-4988
Philipp R. Thies https://orcid.org/0000-0003-3431-8423

REFERENCES

1. Schlipf D, Simley E, Lemmer F, Pao L, Cheng PW. Collective pitch feedforward control of floating wind turbines using LIDAR. In: 25th ISOPE International Ocean and Polar Engineering Conference. ISOPE; 2015. ISOPE-I-15-755.
2. Navalkar ST, van Wingerden J, Fleming PA, Van Kuik G. Integrating robust LIDAR-based feedforward with feedback control to enhance speed regulation of floating wind turbines. In: 2015 American Control Conference (ACC). IEEE; 2015:3070-3075.
3. Schlipf D, Lemmer F, Raach S. Multi-variable feedforward control for floating wind turbines using LIDAR. In: 30th ISOPE International Ocean and Polar Engineering Conference. ISOPE; 2020. ISOPE-I-20-1174.
4. Larsen TJ, Hanson TD. A method to avoid negative damped low frequent tower vibrations for a floating, pitch controlled wind turbine. *J Phys: Conf Ser*. 2007;75(1):12073.
5. Yu W, Lemmer F, Schlipf D, et al. Evaluation of control methods for floating offshore wind turbines. *J Phys: Conf Ser*. 2018;1104(1):12033.
6. Fischer B. Reducing rotor speed variations of floating wind turbines by compensation of non-minimum phase zeros. *IET Renew Power Gen*. 2013;7(4): 413-419.
7. Jonkman J, Butterfield S, Musial W, Scott G. Definition of a 5-MW Reference Wind Turbine for Offshore System Development. Tech. Rep. NREL/TP-500-38060, NREL; 2009.
8. MingYang. Leading innovation: MingYang Smart Energy launches MySE 16.0-242, the world's largest offshore hybrid drive wind turbine. URL: http://www.myse.com.cn/en/jtxw/info.aspx?itemid=825; 2021.
9. Gaertner E, Rinker J, Sethuraman L, et al. Definition of the IEA-Wind 15-Megawatt Offshore Reference Wind Turbine. Tech. Rep. NREL/TP-5000-75698, NREL; 2020.
10. Allen C, Viscelli A, Dagher H, et al. Definition of the UMaine VolturnUS-S Reference Platform Developed for the IEA-Wind 15-Megawatt Offshore Reference Wind Turbine. Tech. Rep. NREL/TP-5000-76773, NREL; 2020.
11. Schlipf D, Guo F, Raach S, Lemmer F. A tutorial on LIDAR-assisted control for floating offshore wind turbines. In: 2023 American Control Conference (ACC). IEEE; 2023:2536-2541.
12. Guo F, Schlipf D. Assessing LIDAR-assisted feedforward and multivariable feedback controls for large floating wind turbines. *Wind Energy Sci Discuss*. 2023;2023:1-25.
13. Bossanyi EA. Individual blade pitch control for load reduction. *Wind Energy*. 2003;6(2):119-128.
14. Namik H, Stol K. Individual blade pitch control of floating offshore wind turbines. *Wind Energy*. 2010;13(1):74-85.
15. Schlipf D, Schuler S, Grau P, Allgöwer F, Kühn M. *Look-Ahead Cyclic Pitch Control Using LIDAR*: University of Stuttgart; 2010.
16. Raach S, Schlipf D, Sandner F, Cheng PW. Nonlinear model predictive control of floating wind turbines with individual pitch control. In: 2014 American control conference (ACC). IEEE; 2014:4434-4439.
17. Dunne F, Pao L, Wright A, Jonkman B, Kelley N. Combining standard feedback controllers with feedforward blade pitch control for load mitigation in wind turbines. In: 48th AIAA Aerospace Sciences Meeting Including the New Horizons Forum and Aerospace Exposition. American Institute of Aeronautics and Astronautics; 2010:250.
18. Dunne F, Schlipf D, Pao L, et al. Comparison of two independent LIDAR-based pitch control designs. In: 50th AIAA Aerospace Sciences Meeting Including the New Horizons Forum and Aerospace Exposition. American Institute of Aeronautics and Astronautics; 2012:1151.
19. NREL. OpenFAST v3.5.0. URL: https://github.com/OpenFAST/openfast/releases/tag/v3.5.0; 2023.
20. Abbas NJ, Zalkind DS, Pao L, Wright A. A reference open-source controller for fixed and floating offshore wind turbines. *Wind Energy Sci*. 2022;7(1): 53-73.
21. NREL. OpenFAST v3.4.0. https://github.com/OpenFAST/openfast/tree/v3.4.0; 2022.
22. Schlipf D, Trujillo JJ, Basterra V, Kühn M. *Development of a Wind Turbine LIDAR Simulator*. University of Stuttgart; 2009.
23. Guo F, Schlipf D, Zhu H, Platt A, Cheng PW, Thomas F. Updates on the OpenFAST LIDAR simulator. *J Phys: Conf Ser*. 2022;2265(4):42030.
24. Guo F, Schlipf D, Cheng PW. Evaluation of LIDAR-assisted wind turbine control under various turbulence characteristics. *Wind Energy Sci*. 2023;8(2): 149-171.
25. Taylor GI. The spectrum of turbulence. *Proc R Soc London Ser A-Math Phys Sci*. 1938;164(919):476-490.
26. Gaertner E, Rinker J, Sethuraman L, et al. IEA-15-240-RWT. https://github.com/IEAWindTask37/IEA-15-240-RWT; 2022.
27. Magar KT, Balas MJ, Frost S. Direct adaptive control for individual blade pitch control of wind turbines for load reduction. *J Intell Material Syst Struct*. 2015;26(12):1564-1572.
28. Schlipf D. *LIDAR-Assisted Control Concepts for Wind Turbines*. University of Stuttgart; 2016.
29. Held DP, Mann J. LIDAR estimation of rotor-effective wind speed—an experimental comparison. *Wind Energy Sci*. 2019;4(3):421-438.
30. MathWorks. cpsd. https://uk.mathworks.com/help/signal/ref/cpsd.html; 2023.
31. MathWorks. pwelch. https://uk.mathworks.com/help/signal/ref/pwelch.html; 2023.
32. Kelley ND, Jonkman BJ. Overview of the TurbSim Stochastic Inflow Turbulence Simulator. Tech. Rep. NREL/TP-500-36971, NREL; 2005.

33. Pao LY, Johnson KE. A tutorial on the dynamics and control of wind turbines and wind farms. In: 2009 American Control Conference (ACC). IEEE; 2009:2076-2089.

34. IEC 61400-3-1:2019—Wind Energy Generation Systems—Part 3-1: Design Requirements for Fixed Offshore Wind Turbines, British Standards Institution; 2019. Tech. Rep.